Coherent ultra-broadband laser-assisted injection radiation from a laser plasma accelerator: Supplementary Material

B. Miao, L. Feder, J. Elle, A. J. Goers, D. Woodbury, F. Salehi, J.K. Wahlstrand, and H. M. Milchberg

Institute for Research in Electronics and Applied Physics, University of Maryland, College Park, MD 20742

1. Measurement of supercontinuum (SC) spectral phase

The spectral phase of the supercontinuum is measured by measuring probe pulse spectrum due to flash induced cross phase modulation as a function of delay [1] as shown in Figure S1. Using a 4th order polynomial fit, we extract the spectral phase to be $\phi(\omega) = \sum_{n=0}^{4} \beta_n(\omega - \omega_0)^n$, where $\beta_2 = 1570 \pm 52\ fs^2, \beta_3 = 222 \pm 51 fs^3, \beta_4 = -3 \pm 70\ fs^4, \omega_0 = 3.6\ PHz$.

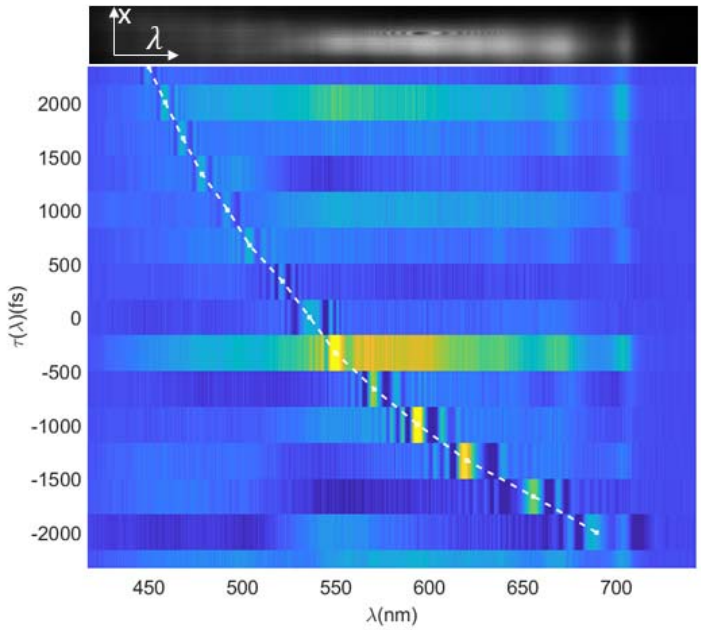

Figure S1. Determination of SC spectral phase. Top: Sample SC spectrogram showing modulation due to cross phase modulation. Bottom: Group delay $\tau(\lambda)$ vs λ using a 25-spectrogram average at each delay.

2. Temporal resolution of single shot supercontinuum spectral interferometry (SSSI)

In our experiment, the temporal resolution of SSSI in method (2) (described in the main text) mainly depends on aberrations in the collection optics and on the intrinsic resolution limit of SSSI. For aberration, we estimate the effect of spherical aberration of the concave silver mirror. According to Eq. (15) of [S2], the total delay caused by spherical aberration of the concave mirror can be estimated as $\tau_{SA} \approx \frac{1.5Ar^4}{\omega_0}$, where A is a dimensionless number characterizing the 3rd

order spherical aberration and r is normalized to the maximum aperture radius. For a concave mirror, it can be shown that $A = -\frac{k_0 a^4}{4R^3}$ [2] where k_0 is the center wave number, a the maximum aperture radius and R the radius of curvature of the concave mirror. In our case, for $\lambda_0 \sim 600\ nm$, $A \sim 24$ (where A is calculated assuming focusing of a collimated beam). This gives $\tau_{SA} = 11.4\ fs$ as an estimate for spherical aberration stretching by the concave mirror.

The limited spectral resolution of the imaging spectrometer in Fig. 1(a) of the main text limits our temporal resolution according to $\tau_w \geq 4\pi|\beta_2 \tau_r^{-1}|$, where τ_r is the maximum available temporal separation between the probe and reference pulse, $\beta_2 = \frac{\partial^2 \phi(\omega)}{\partial \omega^2}$ the first order chirp of the reference pulse [S1]. In our experiment, $\tau_r \approx 1\ ps, \beta_2 \approx 1570\ fs^2$, giving $\tau_w \approx 19.7\ fs$. An estimate of the overall temporal resolution is then $\tau_{res} \approx \sqrt{(\tau_{SA}^2 + \tau_w^2)}$ ≈23 fs.

3. Full data on flash angular distribution and polarization

Figure S2 shows the complete angular and polarization scans for the setup shown in Fig. 1(c) of the main text. The azimuthal observation angle θ (with respect to the pump laser propagation direction) and polarization angle ϕ are varied in 30° steps, where $\phi = 0°$ refers to P-polarization (in the plane of the pump pulse direction, the fibre arm, and the pump polarization), and ϕ=90° describes S-polarization perpendicular to that plane.

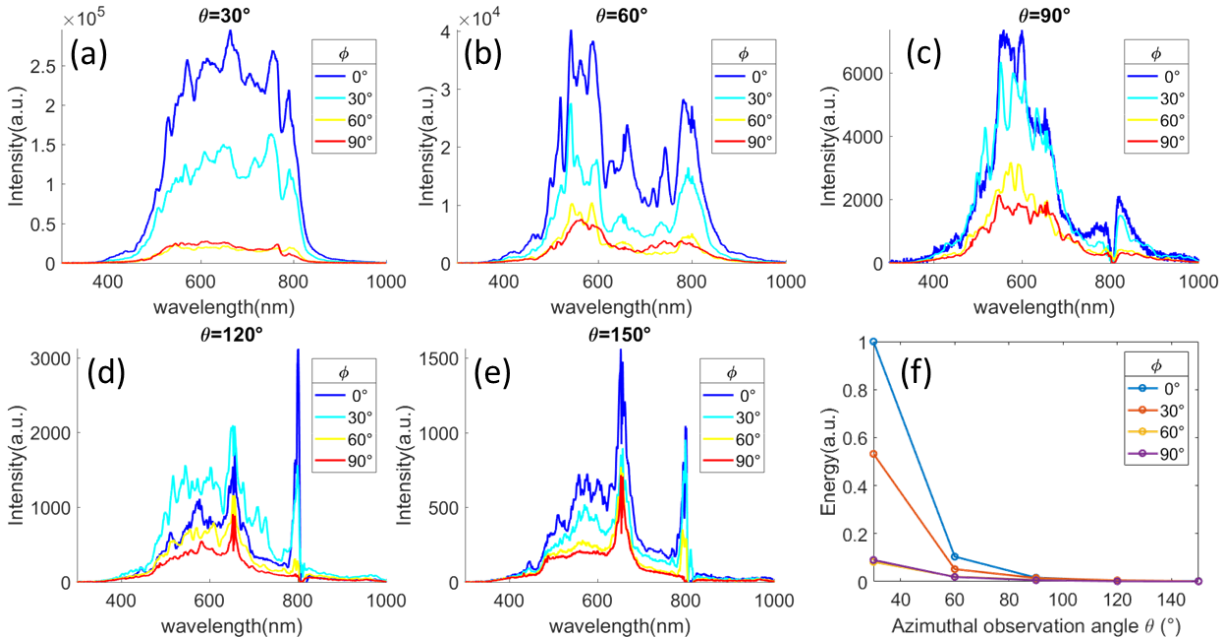

Figure S2. Full scan of flash angular and polarization distribution. (a)-(e) Collected flash spectrum for varying observation angle θ and polarization angle ϕ. $\phi = 0°$ refers to P-polarization and $\phi = 90°$ refers to S-polarization. (f) Relative flash energy integrated over λ=380-1000 nm.

The peak at λ= 656 nm, which is quite strong compared to the rest of the spectrum at the backward angles θ=120° and 150° , is from 3*d*-2*p* hydrogen recombination emission. This emission, which is isotropic and unpolarized, is used to normalize the fibre collection efficiency over its full angular range. The peak near 800nm is weak blue-shifted Thomson scattering of the pump by the plasma, which is negligible compared to the strong flash radiation in the forward

directions, but contributes more significantly to the weaker spectra in the backward directions, but still at an integrated level of <10%. Figure 2(f) shows the collected relative flash energy (integrated over λ=380-1000nm) as a function of θ and ϕ (subtracting out the contributions at λ=656nm). It is seen that the flash angular distribution peaks in the forward direction and decays rapidly with increasing azimuthal angle, and that the emission is dominantly P-polarized. The latter is related to the laser-assisted injection of trapped electrons, as described in Section 5 below.

4. Absolute energy estimate

The fibre spectrometers used in the setup of Fig. 1(c) of the main text are an Ocean Optics HR2000+ (spectral range 200-1100nm) and an Avantes AvaSpec-NIR512 (spectral range 1000-2500nm). As discussed in the main text, there is no flash emission detected beyond ~950nm, so calibration was performed only on the Ocean Optics HR2000+ spectrometer. The full optical path from the source is shown in Fig. S3. All the optics are from Thorlabs, and their part numbers are PFSQ10-03-P01, WP25M-UB, F220SMA-780, MV62L1 and FOFMS respectively. Their transmission is estimated from the Thorlabs website to be 0.98, 0.8, 0.9, 1, 0.8 respectively, so the total transmission is ~56% assuming 100% coupling from the source to the fiber collimator. The fiber collimator is placed ~150 mm away from the source, subtending $\Delta\Omega = 1.8 \times 10^{-3}\ sr$. The fiber spectrometer was calibrated by measuring our Ti:Sapphire oscillator (Coherent Micra) spectrum alongside a Coherent power meter, so the conversion constant between photon number and total spectrometer count is obtained. Then the constant is applied to all the measured spectra for absolute energy measurement.

For calculation of the brightness scale in Fig. 4(c), we use the spatial HWHM of ~2 μm of the spatio-spectral image in Fig. 3(b) of the main text to give a conservative estimate of source area dS. The radiation brightness is then expressed as $B = d^2E/(dSd\Omega)$.

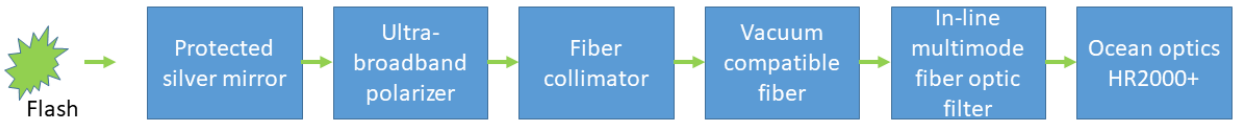

Figure S3. Schematic of angular distribution setup shown in Fig. 1(c) of the main text.

5. Details of PIC simulation

We perform 3D TurboWAVE [3] simulations using a moving window. The number of grid points is $512 \times 512 \times 768$ and the grid size is $\Delta x = \Delta y = 64.5\ nm, \Delta z = 32.3\ nm$. The time step size is $\Delta t = 0.086\ fs$ to follow the Courant condition. For each grid cell there are 8 particles. The laser is linearly polarized in the y direction and propagates in $+z$ direction. The laser pulse has a peak normalized vector potential $a_0 = 1$ at the vacuum focus, pulse width $\tau_{FWHM} = 13.4$ fs and focal spot size $w_{FWHM} = 3.1\ \mu m$. The plasma profile contains a plateau of 13 μm with $N_e/N_{cr} = 0.15$ and 14 μm linear ramps on both sides. To examine which electrons are trapped by the first plasma wave bucket after the laser pulse, we track the trajectories of ~2×10^4 injected electrons with $\gamma - 1 > 0.01$ in a 3D rectangular volume enclosing the accelerated electron bunch as shown in Fig. S4(a) (b), where the colourmap scale is for N_e/N_{cr}.

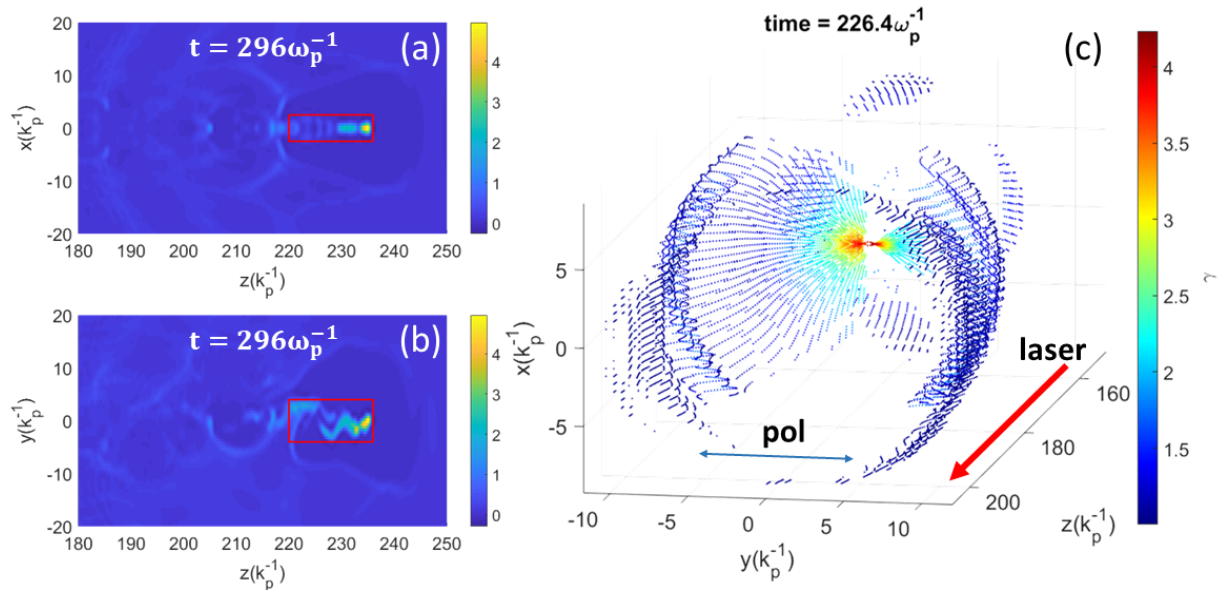

Figure S4. (a)(b) Tracked electrons distributions in *xz* and *yz* planes. The red box represents the rectangular volume for selection of electrons with γ>1. The colormap shows N_e/N_{cr}. (c) 3D spatial distribution of tracked particles in an earlier frame. Each dot represents a tracked particle. The colourmap is in electron γ. It is clear that more accelerated particle trajectories originate near the *yz* plane.

Figure 4(c) shows a snapshot of the tracked and injected particles in the beginning of injection, where each dot represents a particle. The injected particles originate mainly from trajectories in the region of the *yz* plane whereas trajectories in the region of the *xz* plane yield many fewer trapped electrons, a fraction $\lesssim 0.1$. The rotational symmetry is broken by the laser polarization. As discussed in the main text, laser-driven excursions preferentially kick electrons from the plasma wave crest into the accelerating potential well of the plasma wave via polarization-plane (*yz* plane) trajectories. Electrons with laser-driven trajectories in the *yz* plane will become preferentially trapped, whereas electrons do not have such laser-assisted trajectories in the *xz* plane; electrons with *xz* trajectories from the plasma oscillation alone will remain untrapped. Thus, Fig. 4(c) shows a higher density of tracked particles clustered near the *yz* plane, with many fewer near the *xz* plane.

Particle trapping also enables calculation of the vector sum synchrotron radiation and its spectral, angular, and polarization distribution using [4],

$$\left(\frac{d^2I}{d\omega d\Omega}\right)_{\perp,\parallel} = \frac{e^2}{4\pi^2 c}\left|\hat{\boldsymbol{\varepsilon}}^*_{\perp,\parallel}\cdot\int_{-\infty}^{\infty}dt\sum_j \frac{\hat{\boldsymbol{n}}\times\left[\left(\hat{\boldsymbol{n}}-\boldsymbol{\beta}_j\right)\times\dot{\boldsymbol{\beta}}_j\right]}{\left(1-\boldsymbol{\beta}_j\cdot\hat{\boldsymbol{n}}\right)^2}\, e^{i\omega\left(t-\frac{\hat{\boldsymbol{n}}\cdot\boldsymbol{r}_j(t)}{c}\right)}\right|^2 \quad (1),$$

where $\hat{\mathbf{n}}$ is a unit vector pointing from the source to the observation point, $\hat{\boldsymbol{\varepsilon}}_{\perp,\parallel}$ is the unit vector for S- and P-polarization, $\boldsymbol{r}_j, \boldsymbol{\beta}_j$ and $\dot{\boldsymbol{\beta}}_j$ are the position, normalized velocity, and acceleration of electron *j*. In order to simulate the spectral angular distribution of a single flash, all the tracked particles in the red box in figure S4(a)(b) with γ-1>0.01 are used to calculate the radiation spectrum. The computed flash spectrum along the transverse direction in the laser polarization plane ($\theta = 90°$) is shown in Figure S5(b). The spectrum shows modulations reasonably consistent with local plasma period $\tau_p \approx 6.9\, fs$ corresponding to the profile plateau. The

squared magnitude of its Fourier transform in Figure S5(b′) shows a sharp initial burst followed by pulse train structure with approximate ~τ_p spacing, in qualitative agreement with Fig. 3(a) and (b) of the main text. Unlike in that figure, the PIC simulation using Eq. (1) is not space-resolving, so the variable density ramps of the simulation compose a larger fraction of the density profile than in the experiment, contributing to the imperfect lining up of the peaks. At non-transverse observation angles, (a,a′) and (c,c′), the modulations are less clear.

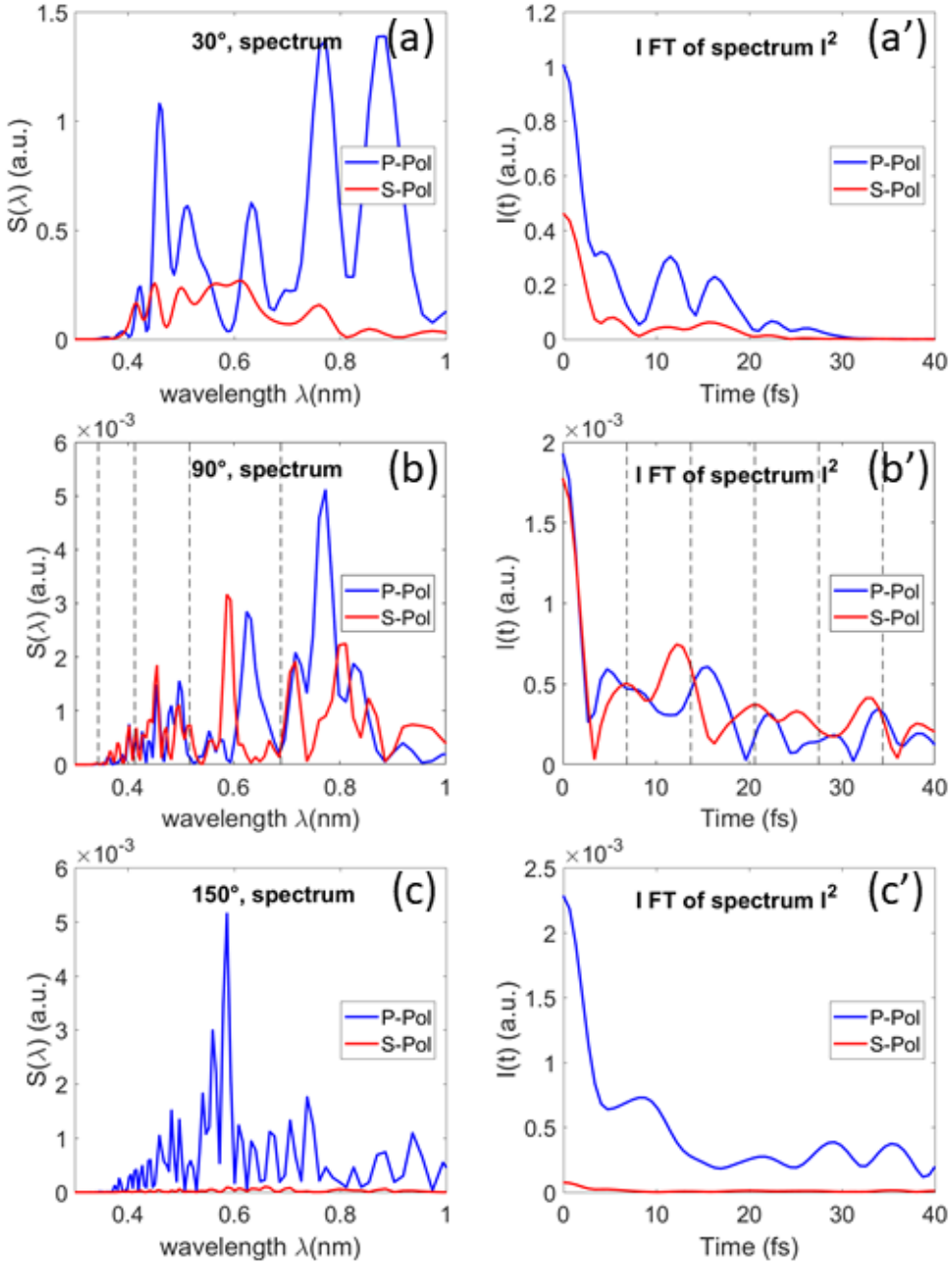

Figure S5. (a)(b)(c) Simulated single flash spectrum in forward, transverse and backward directions ($\theta = 30, 90$ and $135°$) in the laser polarization plane. (a′)(b′)(c′). Magnitude squared of Fourier transform of (a)(b)(c), showing sub-5fs initial flash burst followed by modulations at $\tau_p = 2\pi/\omega_p$, corresponding to laser-assisted injection, which are most clearly seen at $\theta = 90°$. The harmonics of ω_p and oscillations at τ_p are shown as vertical dashed lines. Here the plasma period is $\tau_p \approx 6.9\, fs$.

6. Electron injection movie

The video is extracted from a series of frames of the 3D PIC simulation described in Section 5. The video shows two colour maps. The parula colourmap shows local electron density and the hot colour map shows the normalized instantaneous radiation power of the electron calculated using $P = \frac{2}{3}\frac{e^2}{c}\gamma^6[(\dot{\boldsymbol{\beta}})^2 - (\boldsymbol{\beta} \times \dot{\boldsymbol{\beta}})^2]$ [4]. In the video a tracked electron is shown as a red dot with its time integrated trajectory in hot color map. The trajectory has very small *x*-direction deviation (~0.3 k_p^{-1}) so we only show *yz* plane here. There are two main emission bursts. The first is the injection flash. Later in its trajectory, the trapped electron emits betatron radiation in the forward direction [5].

Link to the video:

https://drive.google.com/file/d/1N04vNMfobGW3RMccu80N_g4vzZQ1loOc/view?usp=sharing

7. Spectrum features of flash emission pulse trains

We model the total electric field radiated by a sequence of N identical flashes separated by $\tau = 2\pi/\omega_p$ as

$$E_{tot}(t) = \sum_{n=1}^{N} E(t - n\tau)e^{-i\omega_0(t-n\tau)},$$

where $E(t)$ is the field envelope for a single flash, idealized as the same at each flash, and ω_0 is a flash central frequency.

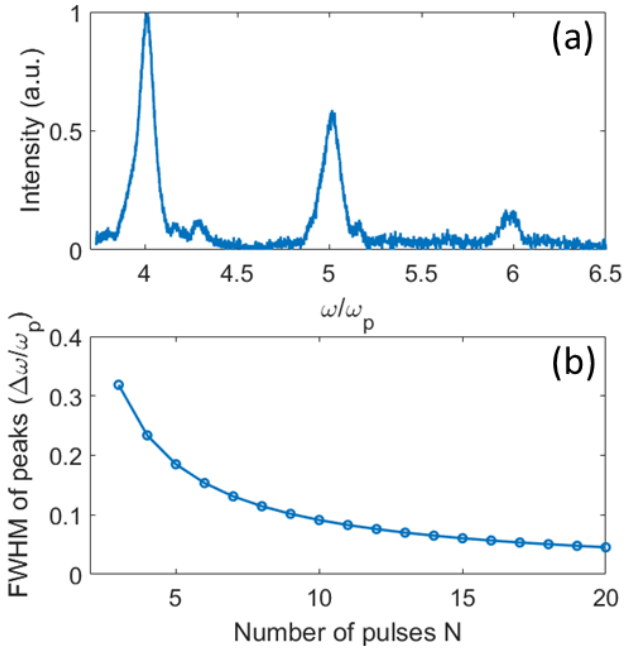

Figure S6. (a) Spatially integrated spectrum along the black line segment (20 rows of CCD camera pixels) in Fig. 3(a), with frequency normalized to local plasma frequency. (b) FWHM of spectrum peak due to interference of a train of N identical pulses separated by $\tau = 2\pi/\omega_p$.

Fourier transforming this expression and forming the square of the magnitude yields the spectrum

$$\left|\tilde{E}_{tot}(\omega)\right|^2 = \left|\tilde{E}(\omega-\omega_0)\right|^2 \frac{\sin^2(\omega N\tau/2)}{\sin^2(\omega\tau/2)}$$

which has peaks at $\omega = m\omega_p$, or at the harmonics of the plasma frequency, agreeing with the experimental spectrum of Fig. S6(a), and where the peak width is $\Delta\omega \sim \omega_p/N$ as plotted in Fig. S6(b). In Fig. 3(a) of the main paper, the width of the spectral peaks $\Delta\omega$ is approximately 1/9 of their ω_p separation as shown in figure S6(a). Thus, N~9.

8. Polarization dependence of laser-assisted injection flash

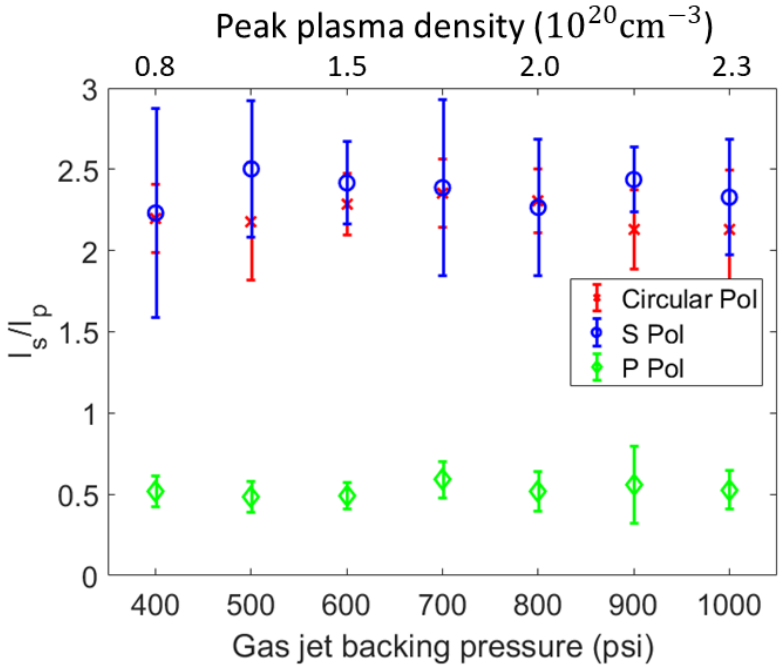

Figure S7. Ratio of S-polarized flash emission to P-polarized emission I_s/I_p as observed at θ=90° for P-polarized, S-polarized, and circularly polarized pump laser. Relative flash energy obtained by integrating CCD camera image of flash. For pump energy 30 mJ, plasma FWHM 450μm, H_2 gas jet. Gas jet backing pressure and corresponding peak plasma density is shown on the horizontal axis.

The flash angular distribution and polarization experiments of the main paper were performed with the pump laser P-polarized, so that the laser-assisted flash radiation is dominantly P-polarized. To test for the dependence of the flash on the pump laser polarization, we inserted either a λ/2 plate or a λ/4 plate before the off-axis parabolic mirror to rotate the linear polarization or to produce circular polarization. Figure S7 shows the ratio I_s/I_p (see main text) measured at θ=90° for S- , P-, and circularly polarized pump-driven flash radiation. Here, in a more qualitative measurement than in the main paper, the relative flash energy was obtained from integrating its image on a CCD camera (see Fig. 1(d) of main paper), which imposes its spectral response, cutting off below ~400 nm and above ~900 nm. In each case, the flash spectrum has little direct contribution from the laser, as seen in Fig. 4 of the main text. For the S-polarization case, it is possible that side Thomson scattering at θ=90°of laser-generated

supercontinuum is contributing to $(I_s/I_p)_{S\,pump} > 1/(I_s/I_p)_{P\,pump}$. The fact that $(I_s/I_p)_{circ\,pump} \lesssim (I_s/I_p)_{S\,pump}$ shows the weak contribution to the flash polarization by orthogonally polarized laser field components.

References

1. J. K. Wahlstrand, S. Zahedpour, and H. M. Milchberg, "*Optimizing the time resolution of supercontinuum spectral interferometry*," J. Opt. Soc. Am. B **33**, 1476 (2016).
2. M. Kempe and W. Rudolph, "*Femtosecond pulses in the focal region of lenses*," Phys. Rev. A **48**, 4721 (1993).
3. D. F. Gordon, "*Improved Ponderomotive Guiding Center Algorithm*," IEEE Trans. Plasma Sci. **35**, 1486 (2007).
4. J. D. Jackson, *Classical Electrodynamics*, 2nd ed. (Wiley, New York, 1975).
5. S. Corde, K. Ta Phuoc, G. Lambert, R. Fitour, V. Malka, and A. Rousse, "*Femtosecond x rays from laser-plasma accelerators*," Rev. Mod. Phys. **85**, 1 (2013).